Science Advances

Supplementary Materials for

Carbon nanotube supported oriented metal organic framework membrane for effective ethylene/ethane separation

Ruicong Wei, Xiaowei Liu, Zongyao Zhou, Cailing Chen, Youyou Yuan, Zhen Li, Xiang Li, Xinglong Dong, Dongwei Lu, Yu Han, Zhiping Lai*

*Corresponding author. Email: zhiping.lai@kaust.edu.sa

The PDF file includes:

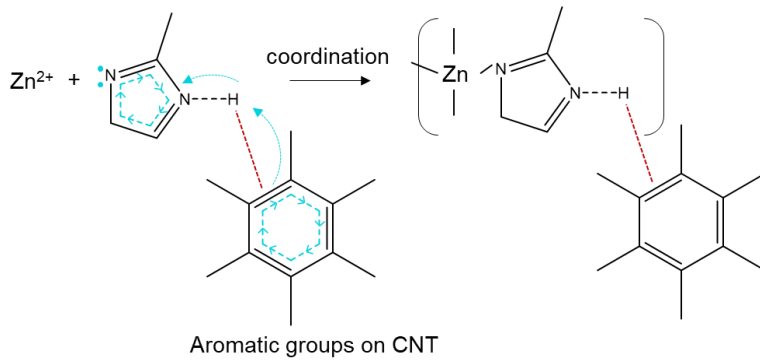Figs. S1 to S18
Tables S1 to S4
References

Other Supplementary Material for this manuscript includes the following:

Movie S1

Fig. S1. Schematic illustration of 2-MIM anchored CNT and associated chemical bond and reactions.
2-MIM was anchored onto CNT via interaction between NH groups and π bond. There could be a charge transfer between 2-MIM and CNT through this interaction (*27*). In the coordination process, the 2-MIM anchored CNT coordinates with zinc ion to form Zn-2-MIM complex.
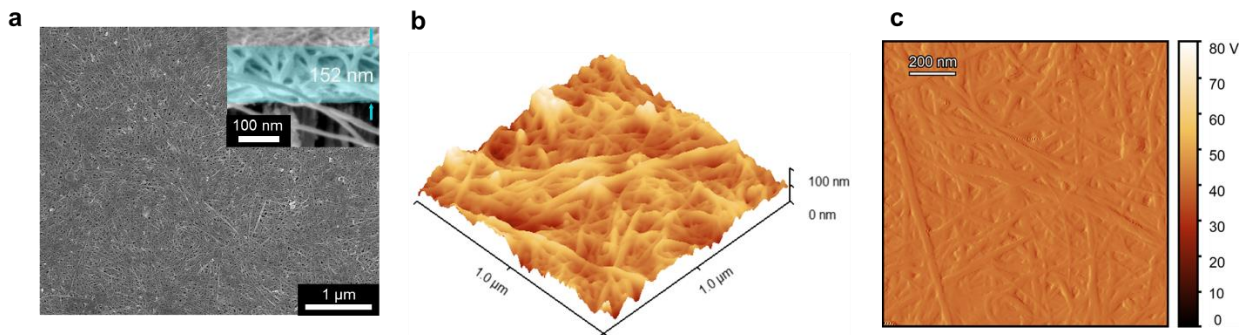

Fig. S2. SEM and AFM characterizations of pristine CNT-AAO substrate.
(a) SEM images of front view and cross view of pristine CNT supported AAO (pristine CNT-AAO). The cross-section view tells the CNT thickness is ~152 nm. (b) AFM Topography (3-D height) image and (c) AFM amplitude image of pristine CNT-AAO.
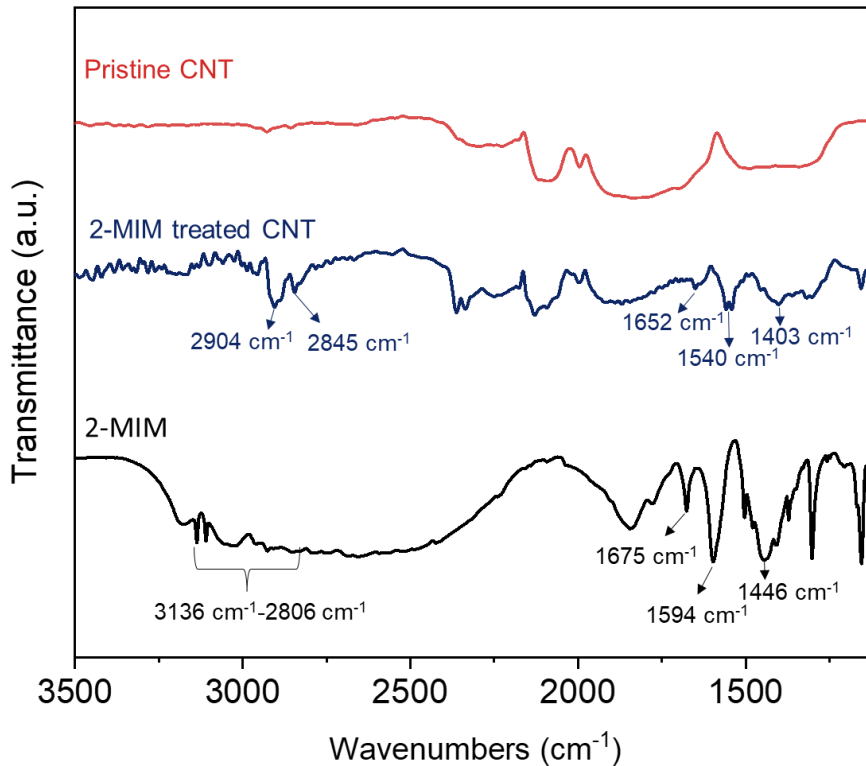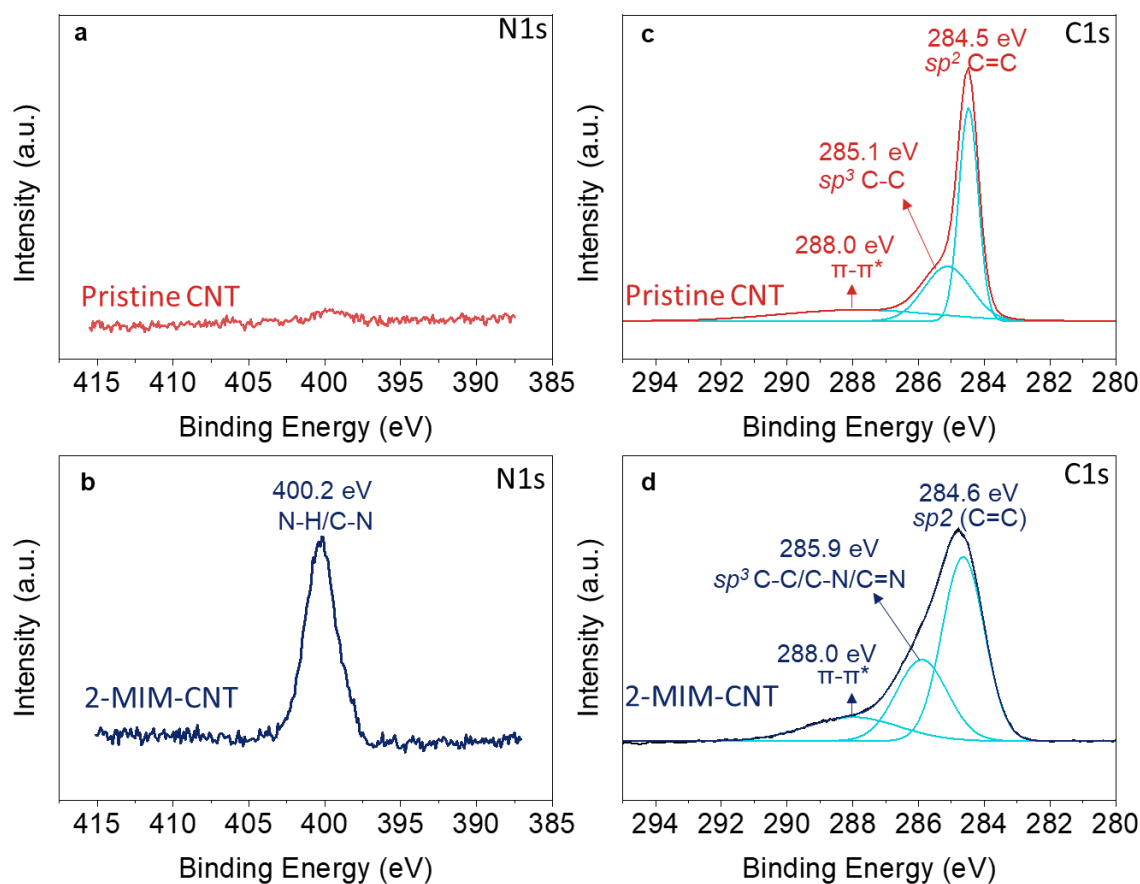
Fig. S3. FTIR patterns of pristine CNT, 2-MIM treated CNT and 2-MIM.
In comparison with pristine CNT, 2-MIM-CNT has extra peaks of 2904 cm^{-1}, 2845 cm^{-1}, 1652 cm^{-1}, 1540 cm^{-1}, and 1403 cm^{-1}. By referring to 2-MIM pattern, the peaks at 2904 cm^{-1} and 2845 cm^{-1} were attributed to C-H stretching, while 1652 cm^{-1}, 1540 cm^{-1} were assigned to C=C and C=N stretching of imidazole ring respectively (*52*). The peak at 1403 cm^{-1} was contributed by C-H bending of -CH$_3$ (*30*). All these peaks demonstrate the existence of 2-MIM on CNT. In addition, all the three peaks (1652 cm^{-1}, 1540 cm^{-1} and 1403 cm^{-1}) of 2-MIM-CNT shifted towards lower wavenumber as comparing with 2-MIM, suggesting the interaction between CNT surface and 2-MIM decreased the C=C and C=N stretching energy and the vibration energy C-H in 2-MIM.
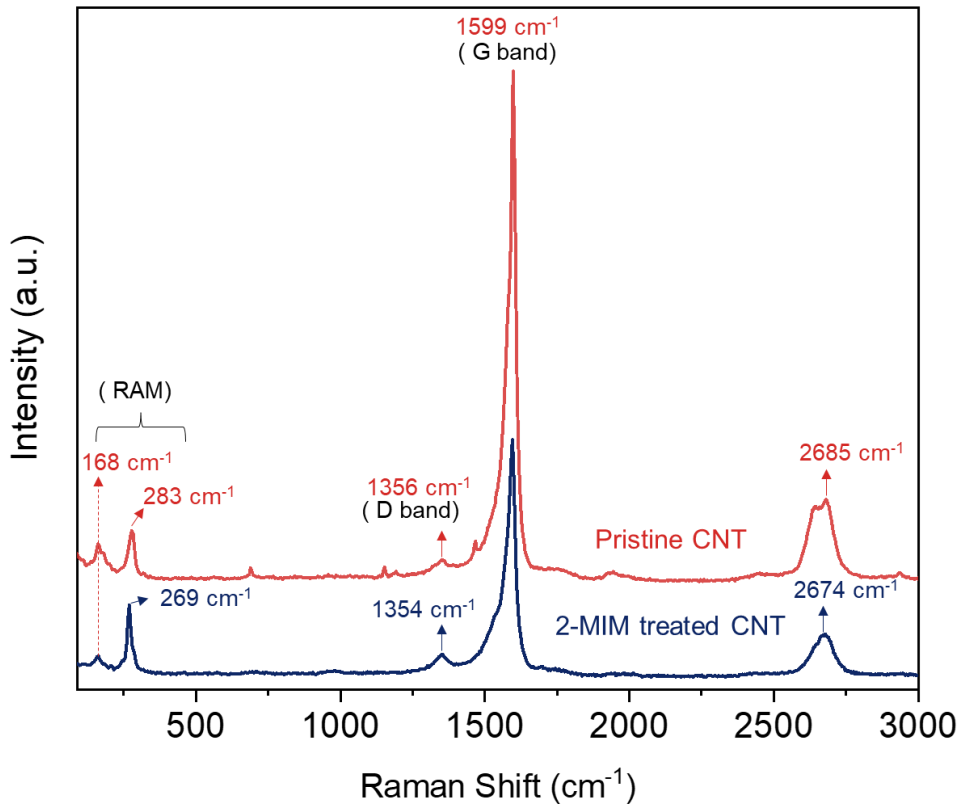
Fig. S4. Raman patterns of pristine CNT and 2-MIM treated CNT.
2-MIM treated CNT (2-MIM-CNT) has five characteristic peaks at 168 cm^{-1}, 269 cm^{-1}, 1354 cm^{-1},1599 cm^{-1} and 2674 cm^{-1}. The peaks at 168 cm^{-1} and 269 cm^{-1} correspond to the radial breathing mode (RAM) attributed by the vibration of the carbon atoms along the radius of the tube, like 'tube breathing' (*53*). The RAM is uniquely observed in single walled CNT, confirming the intrinsic type of CNT used in this study. The peaks at 1599 cm^{-1} and 1354 cm^{-1} are so called G band and D band in CNT (*54*). The G band is contributed by in-plane C-C bond stretching mode (named as 'sp^2 mode') in the hexagonal lattice, while D band is attributed by the activation of 'sp^1 mode' of in-plane C-C stretching caused by surface defects or functionalization (*54*). The peak at 2674 cm^{-1} is the overtone of the D band at 1354 cm^{-1}. As a general consensus in CNT study, the intensity ratio of D band to G band (D/G) gives the purity of the CNT with the ratio proportional to the amount of structural defects or surface functionalization groups (*54*). Comparing with pristine CNT, 2-MIM-CNT has higher D/G, confirming 2-MIM was anchored onto the CNT surface. In addition, we also observed that both D band (1354 cm^{-1}) and RAM peak at 269 cm^{-1} was shifted towards lower frequency as compared with pristine CNT, implying 2-MIM applied a 'tensile strength' on CNT which increased the C-C bond length.

Fig. S5. XPS characterizations of pristine CNT and 2-MIM treated CNT.

XPS patterns of N1s for (a) pristine CNT and (b) 2-MIM treated CNT (2-MIM-CNT). XPS patterns of C1s for (c) pristine CNT and (d) 2-MIM treated CNT. For N1s peaks, it is clear that there is almost no peak for pristine CNT (Fig. S5a) while there is a sharp peak at 400.2 eV for 2-MIM-CNT (Fig. S5b). The signal at 400.2 eV was contributed by a combined contribution of N-H and C-N from 2-MIM (*55*). For C1s patterns of pristine CNT (Fig. S5b), three peaks at 284.5 eV, 285.1 eV and 288.0 eV were assigned to sp^2 C=C, sp^3 C-C, and π–$\pi*$ transition (*56-58*). In comparison, 2-MIM-CNT exhibited peaks at similar positions (284.6 eV, 285.9 eV and 288.0 eV) with a slightly peak shift towards higher binding energy, which is due to the effect of 2-MIM. In particular, the peak at 285.9 eV was contributed by combined effects of sp^3 C-C, C-N and C=N. The area ratio of this peak to sp^2 C=C (284.6 eV) was higher than that of pristine CNT, suggesting there are abundant 2-MIM existed on the surface of CNT. This result is nicely corrected with the associated D/G band ratio comparison in Raman spectra study (Fig. S4).
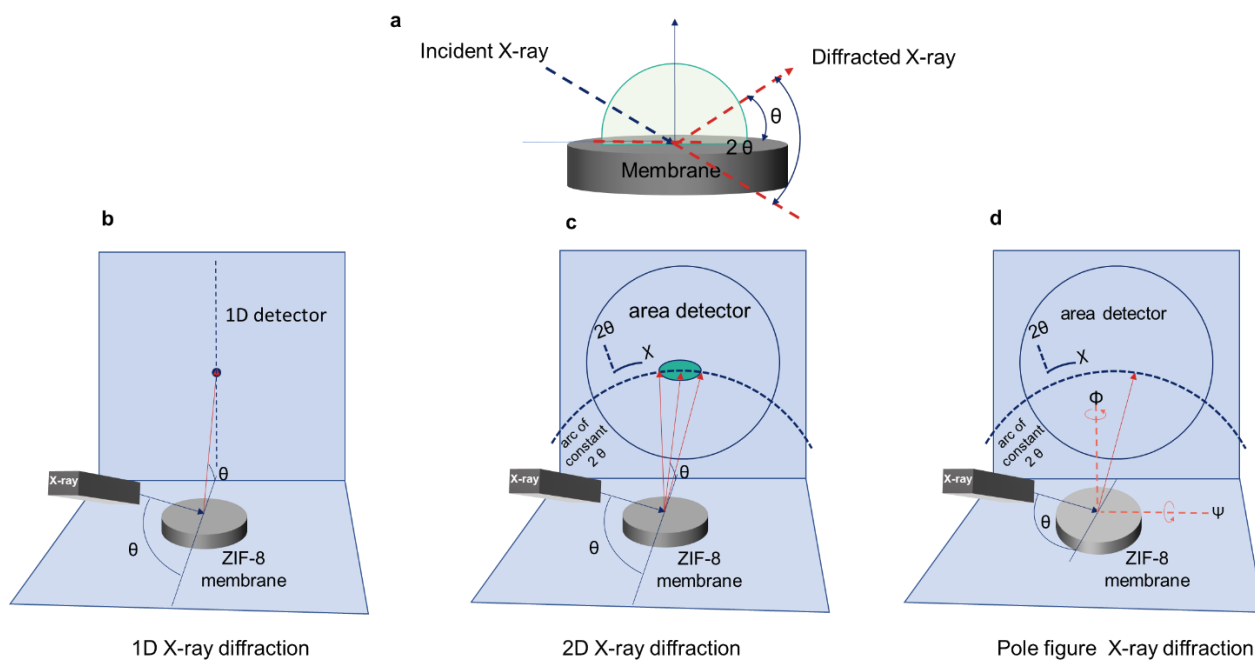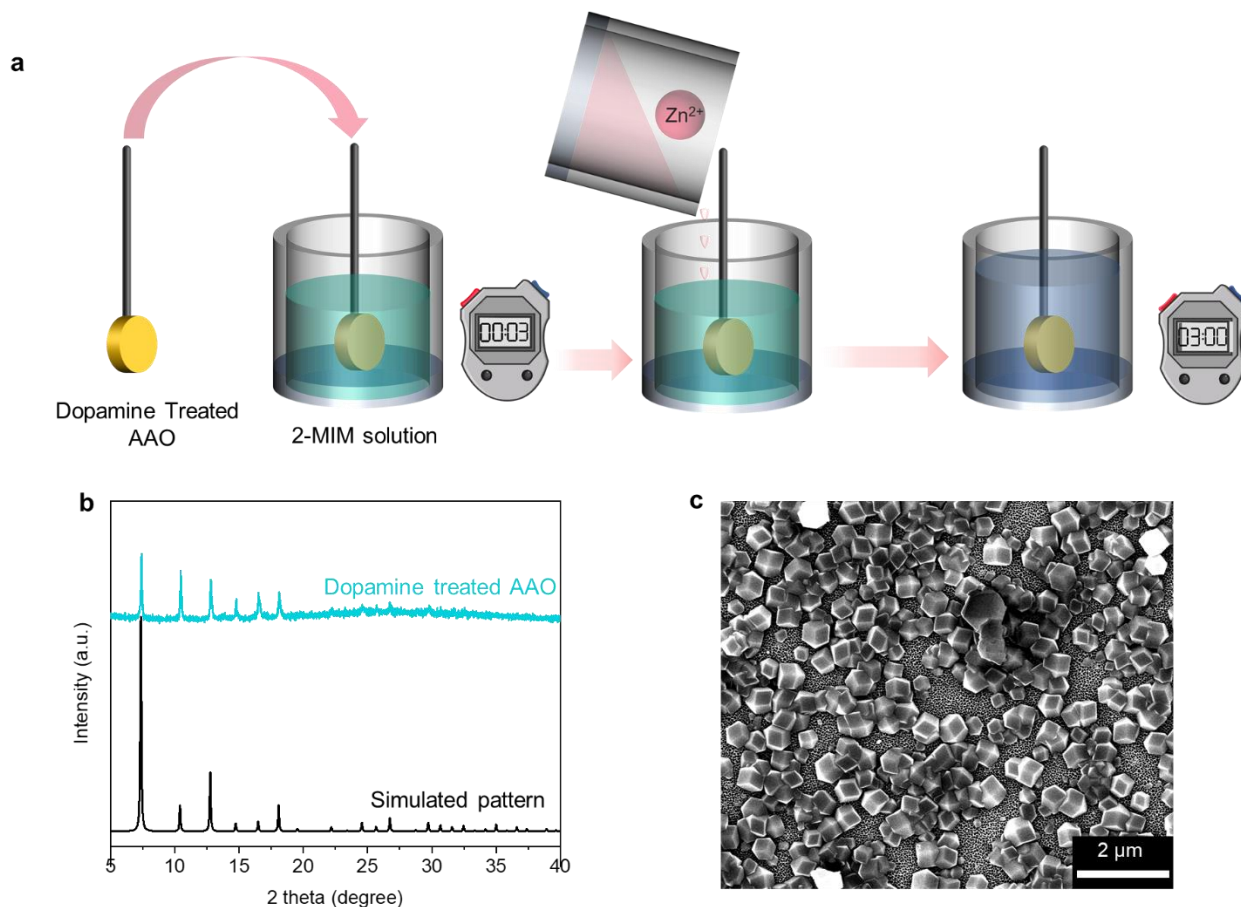
Fig. S6. Schematic illustration of configurations of XRD measurements.
(a) XRD measurement collects the diffracted X-ray signal via Bruker D8 ADVANCE Twin X-ray diffractometer detector, a one-dimensional detector. (b) XRD measurement collects the diffracted X-ray signal via Bruker D8 Eiger diffractometer detector, an area detector. (c) Pole figure measurement was conducted by tiling (Ψ) the membrane samples up to 40 °C and collect the diffracted X-ray signal using a Bruker D8 Eiger diffractometer detector.

Table S1. Crystallographic preferred orientation CPO Indices.

Calculated (CPO) Index for XRD peaks of Randomly oriented membrane (Ran-M) and {100} oriented membrane (100-M). CPO Indices were calculated based on Ref. (*39*). If the CPO index is $\geqslant 1$, then the crystals in the membrane have a preferred (hlk) orientation. If CPO=0~1, the preferred orientation is nominal. In contrast, if CPO is negative, the membrane crystals even prefer (h'l'k') orientation. It is clearly that compared with Ran-M, 100-M has much higher CPO indices of (200) reflection in relation to reflections of 110 ($CPO_{200/110}$) and 211 ($CPO_{200/211}$), demonstrating the highly preferred {100} orientation in 100-M.

CPO Index	Ran-M	100-M
200/110	2.9	115.6
200/211	1.6	81.8
200/220	0.4	7.2
200/310	-0.4	3.1
200/222	0.8	15.5

Fig. S7. Schematic illustration, XRD and SEM results of comparison experiment 1.
(a) Schematic illustration of comparison experiment 1 which firstly immersed dopamine treated AAO in the 2-MIM solution for 3 min followed by in situ growth in ZIF-8 precursor for 3 hours at room temperature. (b) XRD pattern of the resultant sample of dopamine treated AAO after 3 hours reaction compared with simulated pattern of ZIF-8. (c) SEM image the resultant sample of dopamine treated AAO after 3 hours in situ growth in ZIF-8 precursor.
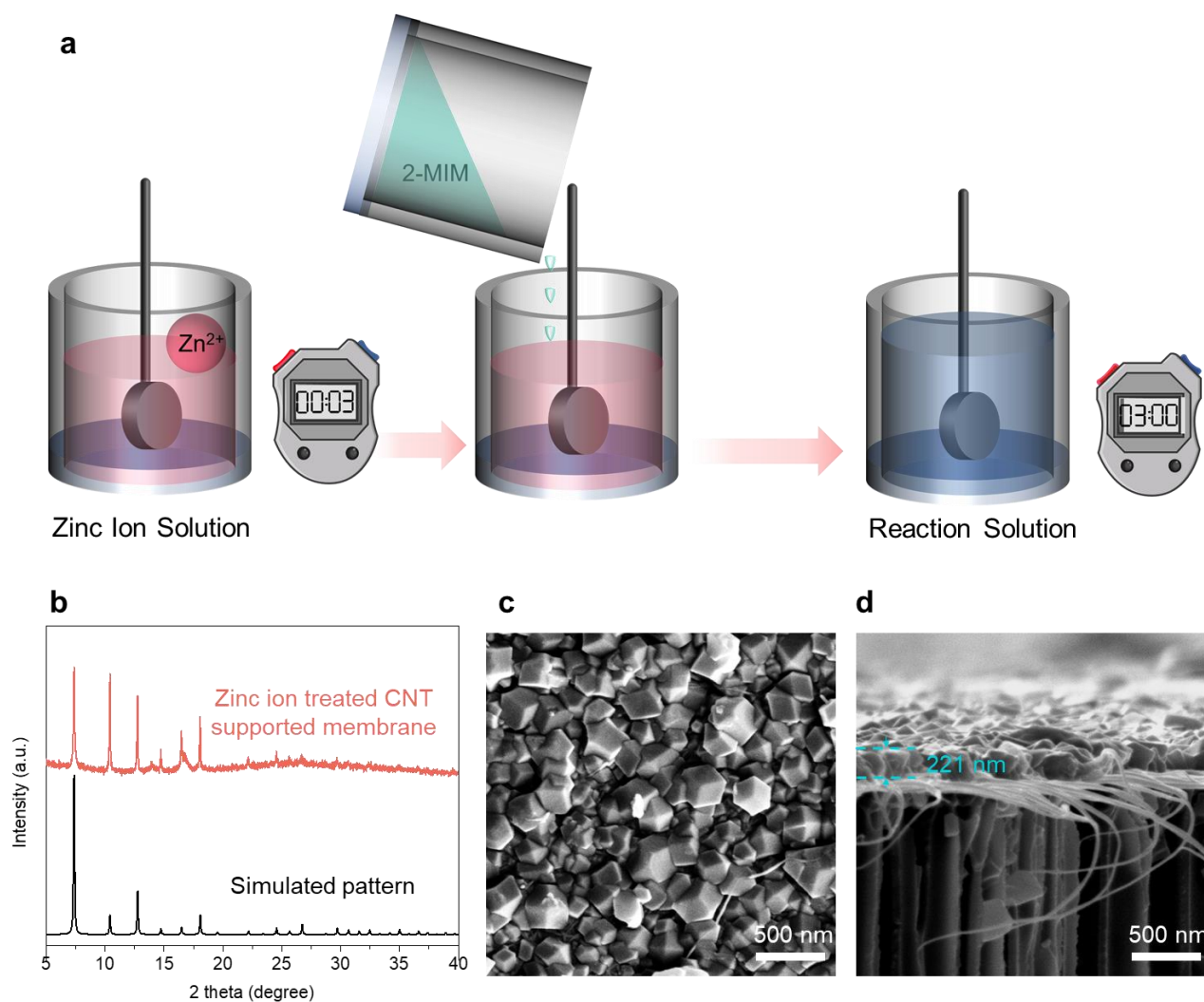
Fig. S8. Schematic illustration, XRD and SEM results of comparison experiment 2.
(a) Schematic illustration of comparison experiment 2. The pristine CNT-AAO substrate was treated with zinc ion solution for 3 min followed by in situ growth in ZIF-8 precursor for 3 hours at room temperature. (b) XRD pattern of the resultant zinc ion treated CNT supported membrane compared with simulated pattern of ZIF-8. (c) Front view of SEM image the resultant zinc ion treated CNT supported membrane. (d) The cross-view SEM image of the resultant zinc ion treated CNT supported membrane.
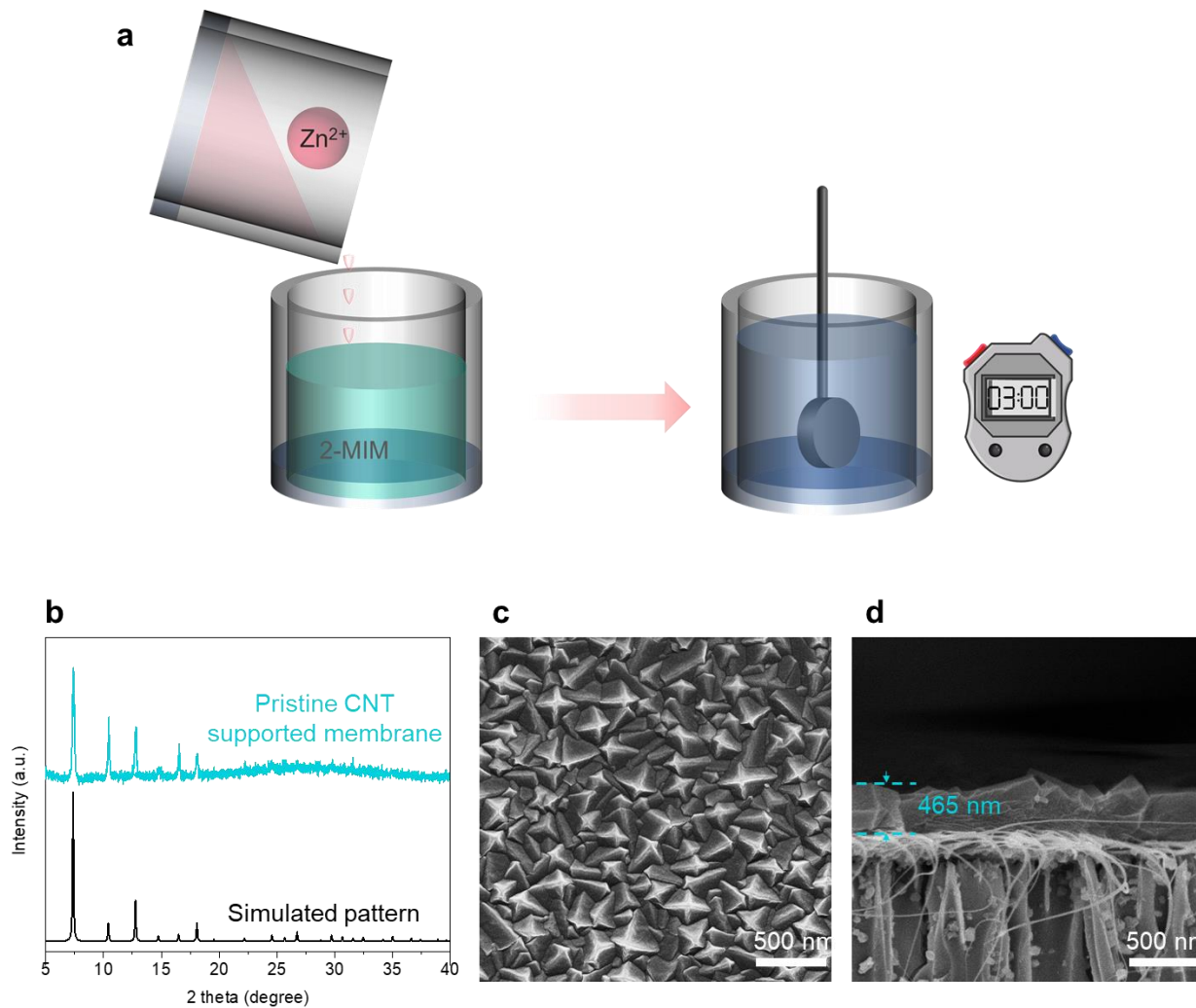
Fig. S9. Schematic illustration, XRD and SEM results of comparison experiment 3.
(a) Schematic illustration of comparison experiment 3. The pristine CNT-AAO substrate was directly immersed into ZIF-8 reaction precursor and subjected to in situ growth for 3 hours at room temperature. (b) XRD pattern of the resultant pristine CNT supported membrane compared with simulated pattern of ZIF-8. (c) The front-view SEM image of the resultant pristine CNT supported membrane. (d) The cross-view SEM image of the resultant pristine CNT supported membrane.
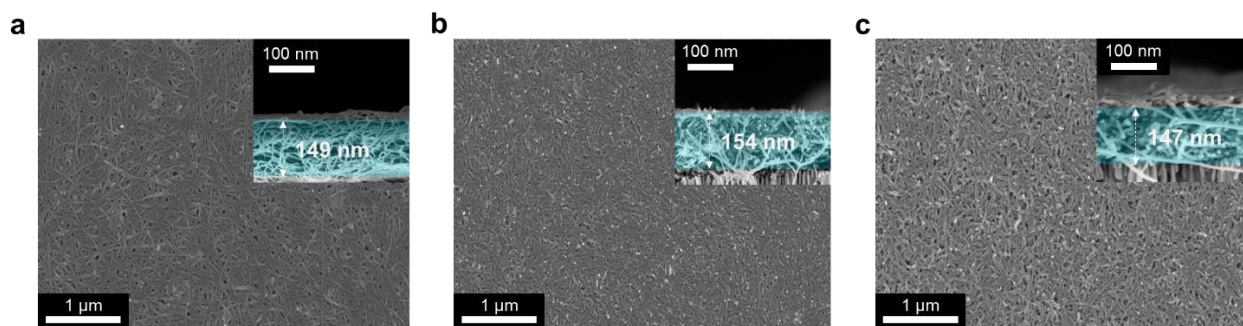
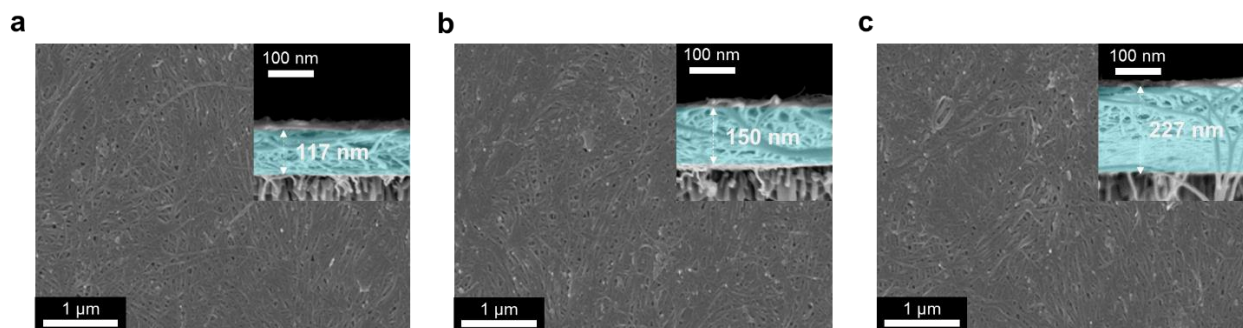**Fig. S10. SEM images of support layer composed of CNT with different outer diameters (ODs).**
The CNT layer was fabricated by vacuum filtering CNT solution of OD size (a) less than 2 nm, (b) less than 8 nm, and (c) 8-15 nm. The front views show the CNT layer have similar packing density while the cross view illustrates the thickness of the CNT layers are similar with the standard deviation less than 5%.


Fig. S11. SEM images of support layer composed of CNT with different thicknesses.
The CNT layer was fabricated by vacuum filtering CNT (OD, less than 2 nm) solution of different amount to form a layer with thickness (a) ~117 nm, (b) ~ 150 nm, and (c) ~227 nm. The front views show the CNT layers have a similar packing density while the cross views give the thickness of the support layers.
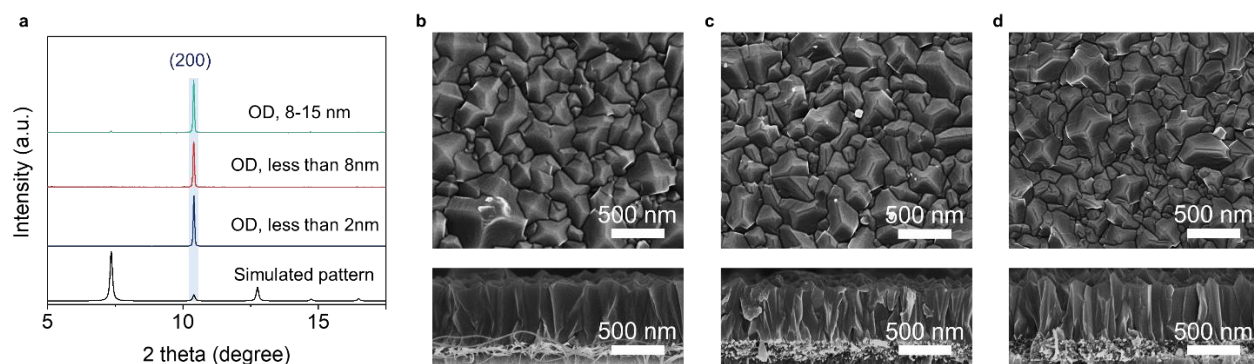
Fig. S12. XRD and SEM imaging characterizations of ZIF-8 membranes supported by CNT layers of different outer diameters (ODs).

(a) XRD patterns of ZIF-8 membranes synthesized using CNT layers of different ODs. All the patterns show (200) orientation is dominant with other peaks visually diminished, suggesting {100} oriented membranes were formed from the CNT of different ODs. SEM images show both front views and cross views of ZIF-8 membranes obtained from CNT OD of (a) less than 2 nm, (b) less than 8 nm, and (c) 8-15 nm. The front views of the three membranes all show characteristic morphology of {100} oriented rhombic dodecahedral crystals. Meanwhile, the cross views of the three membranes show a similar thickness of ~540 nm with less than 5% standard deviation.
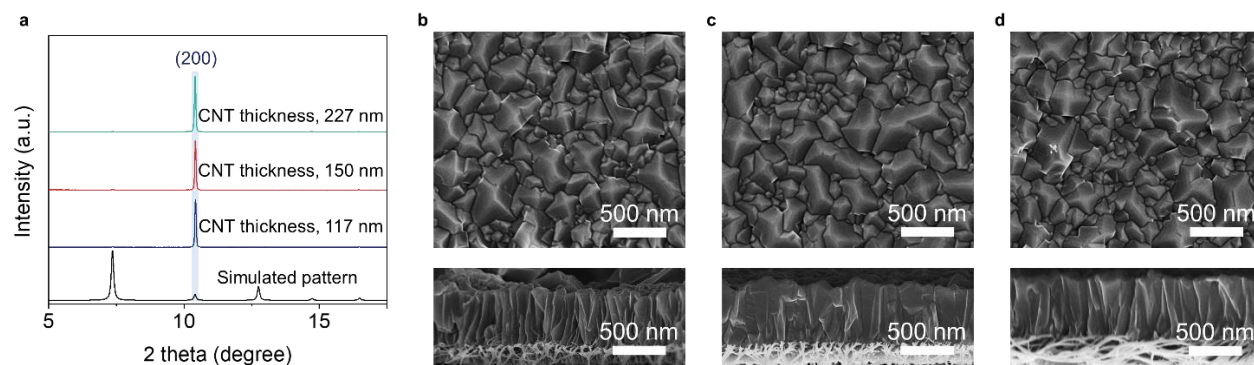
Fig. S13. XRD and SEM imaging characterizations of ZIF-8 membrane supported by CNT layers of different thicknesses.

(a) XRD patterns of ZIF-8 membranes synthesized using CNT layers of different thicknesses. All the patterns show (200) orientation is dominant with other peaks visually diminished, suggesting {100} oriented membranes were formed from CNT of different thicknesses. SEM images show both front views and cross views of ZIF-8 membranes obtained from CNT thickness of (a) ~117 nm, (b) ~150 nm, and (c) 227 nm. The front views of the three membranes all show characteristic morphology of {100} oriented rhombic dodecahedral crystals. Meanwhile, the cross views of the three membranes show a similar thickness of ~540 nm with less than 5% standard deviation.
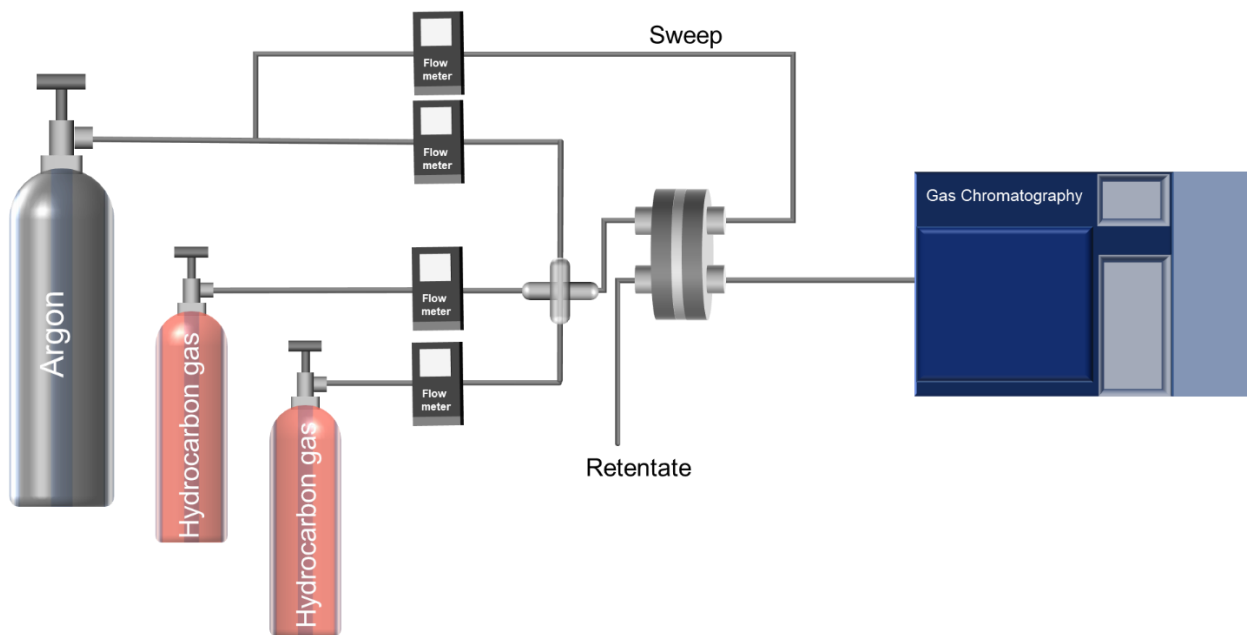
Fig. S14. The setup of Wicke–Kallenbach technique for gas permeation test.
At the feed side to the membrane permeation cell, the mass flow rate of individual hydrocarbon gas was controlled by a flow meter, from which the required gas feed ratio could be manipulated via the flow meters before mixing them to the feed side of the membrane cell. At the permeate side, the permeate hydrocarbon gas mixtures were swept by argon gas and fed into Gas Chromatography (GC) for analysis. The argon gas was used as both sweep gas and flush gas to get rid of all the hydrocarbon gases after one measurement. The mass flow rate of argon gas was controlled by flow meter as well.

Table S2. List of gas molecule size used to test the critical size of 4-memberred window of ZIF-8.

The van der Waals diameter (Å) was used for gas molecule C_2H_4, C_2H_6, C_3H_6 and C_3H_8 while kinetic diameter (Å) was used for nC_4H_{10} and Iso C_4H_{10} (Å) based on Ref. (*11*).

Gas	Molecular diameter (Å)
C_2H_4	3.6
C_2H_6	3.7
C_3H_6	4.0
C_3H_8	4.2
nC_4H_{10}	4.3
Iso C_4H_{10}	5.0
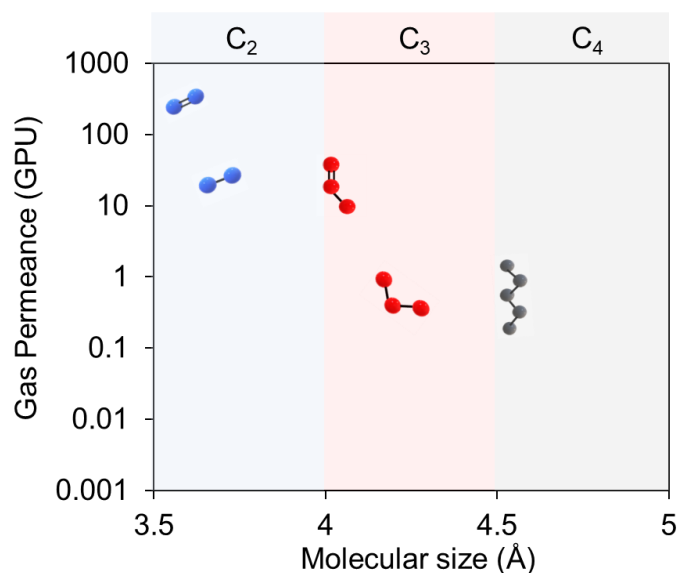
Fig. S15. Gas permeation test of {100} oriented membrane (100-M).

Binary gas permeation test of 100-M of different molecule sizes including C2 (C_2H_4, C_2H_6), C3 (C_3H_6, C_3H_8) and C4 (nC_4H_{10}, $isoC_4H_{10}$). The plot gives the gas permeance of each gas versus molecular size. It is noted that the permeance of $isoC_4H_{10}$ was not plotted in this graph as we didn't detect any $isoC_4H_{10}$ under the GC testing conditions of this study.

Table S3. Gas separation performance of <100> oriented membrane (100-M).
The permeation test was used the setup shown in Fig.S14 at room temperature and 1bar. The test was conducted using binary feed gas mixtures including C_2H_4/C_2H_6, C_3H_6/C_3H_8 and $nC_4H_{10}/isoC_4H_{10}$. The data was plotted in Fig. S15.

Gas	Permeance (GPU)	Flux (10^{-3} mol m^{-2} s^{-1})	Selectivity (feed 50:50)
C_2H_4	244	4.8	
C_2H_6	25.3	0.5	$C_2H_4/C_2H_6 = 9.6$
C_3H_6	18.1	0.36	
C_3H_8	0.45	0.009	$C_3H_6/C_3H_8 = 40.3$
nC_4H_{10}	0.5	0.01	
Iso C_4H_{10}	0	0	$nC_4H_{10}/isoC_4H_{10} =$ unlimited

Table S4. Gas separation performance of randomly oriented membrane（Ran-M).
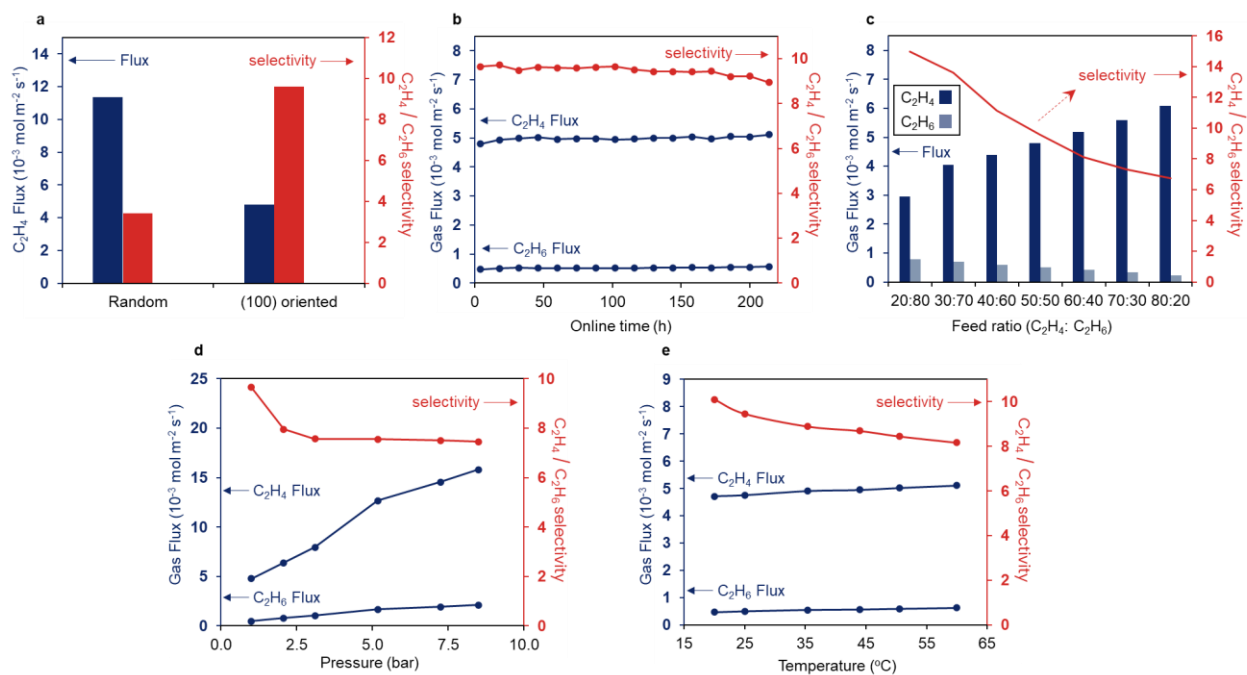The permeation test was used the setup shown in Fig.S14 at room temperature and 1bar. The test was conducted using binary feed gas mixtures including C_2H_4/C_2H_6 and C_3H_6/C_3H_8. The data was plotted in Fig 4a.

Gas	Permeance (GPU)	Flux (10^{-3} mol m^{-2} s^{-1})	Selectivity (feed 50:50)
C_2H_4	581.1	11.4	
C_2H_6	169.9	3.3	$C_2H_4/C_2H_6 = 3.4$
C_3H_6	53.4	1.05	
C_3H_8	0.349	0.007	$C_3H_6/C_3H_8 = 153$

Fig. S16. Gas separation performances of {100} oriented membrane.

(a) C_2H_4/C_2H_6 separation performance of 100-M compared with Ran-M. (b) Long-term stability of 100-M for C_2H_4/C_2H_6 separation at room temperature and 1 bar. (c) C_2H_4/C_2H_6 separation performance of 100-M at different feed ratios. (d) C_2H_4/C_2H_6 separation performances of 100-M as a function of feed pressure. (e) C_2H_4/C_2H_6 separation performances of 100-M as a function of temperature. All the gas transport was reported as flux in the unit of 10^{-3} mol m^{-2} s^{-1}.

(a) Curvature = 109 m⁻¹ 100-M

(b) Curvature = 15 m⁻¹ Pristine AAO
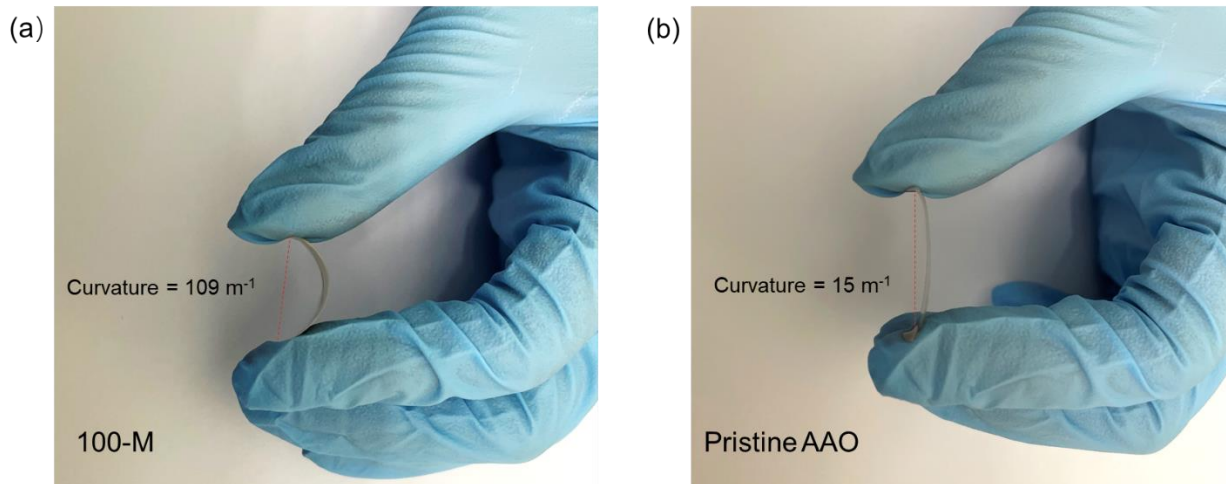
Fig. S17. Images of bending the membrane and pristine AAO support to a specific curvature before breaking apart.

(a) {100} oriented membrane (100-M) could sustain the bending to a curvature of ~ 109 m⁻1 without affecting the separation performances as shown in Fig. 4 (f) in the main text. (b) As a comparison test, pristine AAO could sustain a bending to a curvature ~15 m⁻¹ before breaking apart.
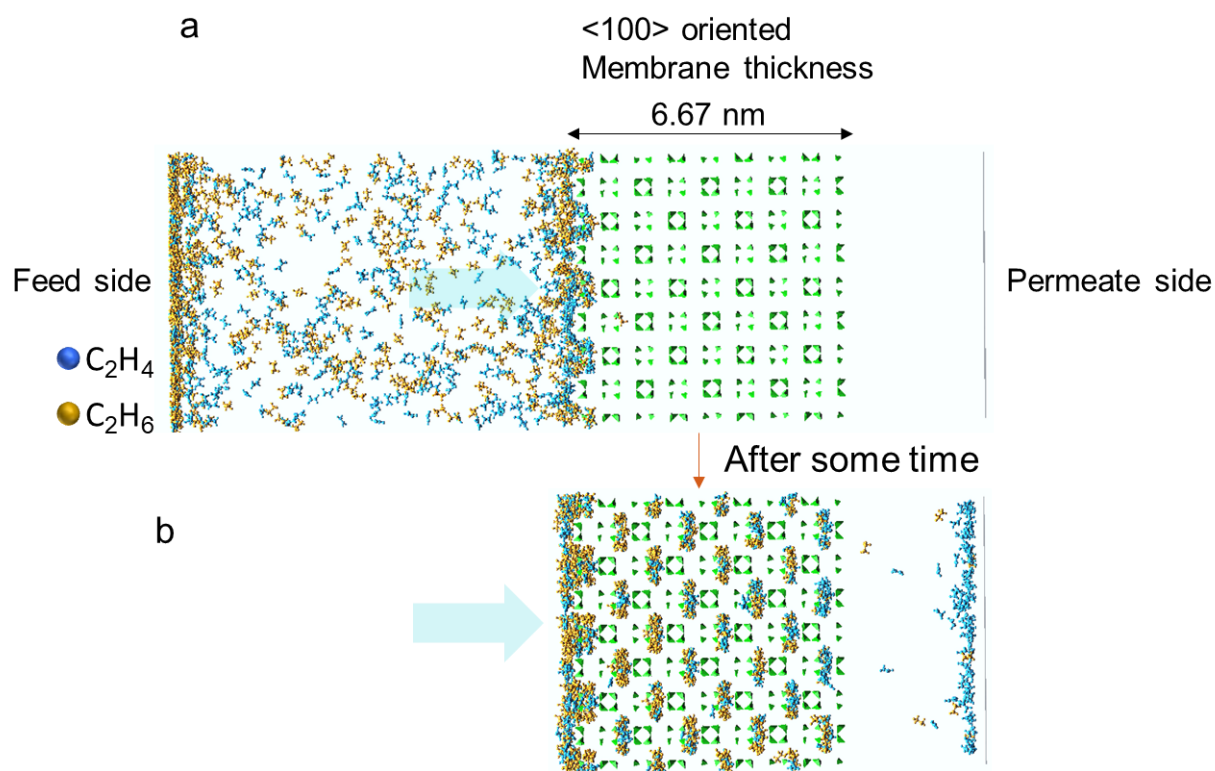
Fig. S18. Molecule dynamic simulation process.
(a) Schematic illustration of molecular dynamic simulation process before mixture of C_2H_4 and C_2H_6 (50: 50 molar ratio) being fed into the membrane along <100> direction. The membrane was composed of $4 \times 4 \times 4$ unit cells with a membrane thickness of 6.67 nm. (b) A snapshot of the separation process after the binary gas mixture being fed into the membrane.

REFERENCES AND NOTES

1. M. Safaei, M. M. Foroughi, N. Ebrahimpoor, S. Jahani, A. Omidi, M. Khatami, A review on metal-organic frameworks: Synthesis and applications. *TrAC Trends Anal. Chem.* **118**, 401–425 (2019).

2. M. R. Abdul Hamid, Y. Qian, R. Wei, Z. Li, Y. Pan, Z. Lai, H.-K. Jeong, Polycrystalline metal-organic framework (MOF) membranes for molecular separations: Engineering prospects and challenges. *J. Membr. Sci.* **640**, 119802 (2021).

3. Z. Lai, G. Bonilla, I. Diaz, J. G. Nery, K. Sujaoti, M. A. Amat, E. Kokkoli, O. Terasaki, R. W. Thompson, M. Tsapatsis, D. G. Vlachos, Microstructural optimization of a zeolite membrane for organic vapor separation. *Science* **300**, 456–460 (2003).

4. Y. Sun, Y. Liu, J. Caro, X. Guo, C. Song, Y. Liu, In-plane epitaxial growth of highly *c*- oriented NH_2-MIL-125(Ti) membranes with superior H2/CO_2 selectivity. *Angew. Chem. Int. Ed.* **57**, 16088–16093 (2018).

5. Y. Liu, Y. Ban, W. Yang, Microstructural engineering and architectural design of metal–organic framework membranes. *Adv. Mater.* **29**, 1606949 (2017).

6. M. A. Snyder, M. Tsapatsis, Hierarchical nanomanufacturing: From shaped zeolite nanoparticles to high-performance separation membranes. *Angew. Chem. Int. Ed.* **46**, 7560–7573 (2007).

7. Y. Pan, T. Li, G. Lestari, Z. Lai, Effective separation of propylene/propane binary mixtures by ZIF-8 membranes. *J. Membr. Sci.* **390**, 93–98 (2012).

8. R. Wei, H. Y. Chi, X. Li, D. Lu, Y. Wan, C. W. Yang, Z. Lai, Aqueously cathodic deposition of ZIF-8 membranes for superior propylene/propane separation. *Adv. Funct. Mater.* **30**, 1907089 (2020).

9. A. J. Brown, N. A. Brunelli, K. Eum, F. Rashidi, J. R. Johnson, W. J. Koros, C. W. Jones, S. Nair, Interfacial microfluidic processing of metal-organic framework hollow fiber membranes. *Science* **345**, 72–75 (2014).

10. A. Knebel, B. Geppert, K. Volgmann, D. I. Kolokolov, A. G. Stepanov, J. Twiefel, P. Heitjans, D. Volkmer, J. Caro, Defibrillation of soft porous metal-organic frameworks with electric fields. *Science* **358**, 347–351 (2017).

11. C. Zhang, R. P. Lively, K. Zhang, J. R. Johnson, O. Karvan, W. J. Koros, Unexpected molecular sieving properties of zeolitic imidazolate framework-8. *J. Phys. Chem. Lett.* **3**, 2130–2134 (2012).

12. B. Zheng, Y. Pan, Z. Lai, K.-W. Huang, Molecular dynamics simulations on gate opening in ZIF-8: Identification of factors for ethane and propane separation. *Langmuir* **29**, 8865–8872 (2013).

13. C. L. Hobday, C. H. Woodall, M. J. Lennox, M. Frost, K. Kamenev, T. Düren, C. A. Morrison, S. A. Moggach, Understanding the adsorption process in ZIF-8 using high pressure crystallography and computational modelling. *Nat. Commun.* **9**, 1429 (2018).

14. M. Fischer, R. G. Bell, Interaction of hydrogen and carbon dioxide with sod-type zeolitic imidazolate frameworks: A periodic DFT-D study. *CrstEngComm* **16**, 1934–1949 (2014).

15. Y. Liu, G. Zeng, Y. Pan, Z. Lai, Synthesis of highly c-oriented ZIF-69 membranes by secondary growth and their gas permeation properties. *J. Membr. Sci.* **379**, 46–51 (2011).

16. Y. Yoo, Z. Lai, H.-K. Jeong, Fabrication of MOF-5 membranes using microwave-induced rapid seeding and solvothermal secondary growth. *Microp. Mesop. Mater.* **123**, 100–106 (2009).

17. Y. Sun, C. Song, X. Guo, Y. Liu, Concurrent manipulation of out-of-plane and regional in-plane orientations of NH2-UiO-66 membranes with significantly reduced anisotropic grain boundary and superior H2/CO$_2$ separation performance. *ACS Appl. Mater. Interfaces* **12**, 4494–4500 (2020).

18. J. Yan, Y. Sun, T. Ji, L. Liu, M. Zhang, Y. Liu, Cooperative defect tailoring: A promising protocol for exceeding performance limits of state-of-the-art MOF membranes. *J. Membr. Sci.* **635**, 119515 (2021).

19. A. Van der Drift, Evolutionary selection, a principle governing growth orientation in vapour-deposited layers. *Philips Res. Rep.* **22**, 267–288 (1967).

20. A.-J. Bons, P. D. Bons, The development of oblique preferred orientations in zeolite films and membranes. *Microp. Mesop. Mater.* **62**, 9–16 (2003).

21. S. Friebe, B. Geppert, F. Steinbach, J. R. Caro, Metal–organic framework UiO-66 layer: A highly oriented membrane with good selectivity and hydrogen permeance. *ACS Appl. Mater. Interfaces* **9**, 12878–12885 (2017).

22. H. Bux, A. Feldhoff, J. Cravillon, M. Wiebcke, Y.-S. Li, J. Caro, Oriented zeolitic imidazolate framework-8 membrane with sharp H_2/C_3H_8 molecular sieve separation. *Chem. Mater.* **23**, 2262–2269 (2011).

23. O. Shekhah, H. Wang, S. Kowarik, F. Schreiber, M. Paulus, M. Tolan, C. Sternemann, F. Evers, D. Zacher, R. A. Fischer, C. Wöll, Step-by-step route for the synthesis of metal−organic frameworks. *J. Am. Chem. Soc.* **129**, 15118–15119 (2007).

24. O. Shekhah, R. Swaidan, Y. Belmabkhout, M. Du Plessis, T. Jacobs, L. J. Barbour, I. Pinnau, M. Eddaoudi, The liquid phase epitaxy approach for the successful construction of ultra-thin and defect-free ZIF-8 membranes: Pure and mixed gas transport study. *Chem. Commun.* **50**, 2089–2092 (2014).

25. E. P. Valadez Sánchez, H. Gliemann, K. Haas-Santo, C. Wöll, R. Dittmeyer, ZIF-8 SURMOF membranes synthesized by Au-assisted liquid phase epitaxy for application in gas separation. *Chem. Ing. Tech.* **88**, 1798–1805 (2016).

26. Y. Geng, T. Takatani, E. G. Hohenstein, C. D. Sherrill, Accurately characterizing the π−π interaction energies of indole−benzene complexes. *J. Phys. Chem. A* **114**, 3576–3582 (2010).

27. S. M. Brülls, V. Cantatore, Z. Wang, P. L. Tam, P. Malmberg, J. Stubbe, B. Sarkar, I. Panas, J. Mårtensson, S. Eigler, Evidence for electron transfer between graphene and non-covalently bound π-systems. *Chem. A Eur. J.* **26**, 6694–6702 (2020).

28. Y. Pan, Y. Liu, G. Zeng, L. Zhao, Z. Lai, Rapid synthesis of zeolitic imidazolate framework-8 (ZIF-8) nanocrystals in an aqueous system. *Chem. Commun.* **47**, 2071–2073 (2011).

29. P. Y. Moh, "Crystal growth of the metal-organic framework ZIF-8", thesis, University of Manchester (2012).

30. S. Lee, Y. Lei, D. Wang, C. Li, J. Cheng, J. Wang, W. Meng, M. Liu, The study of zeolitic imidazolate framework (ZIF-8) doped polyvinyl alcohol/starch/methyl cellulose blend film. *Polymers* **11**, 1986 (2019).

31. D. Liu, X. Ma, H. Xi, Y. S. Lin, Gas transport properties and propylene/propane separation characteristics of ZIF-8 membranes. *J. Membr. Sci.* **451**, 85–93 (2014).

32. J.-H. Chen, W.-S. Luo, Flexural properties and fracture behavior of nanoporous alumina film by three-point bending test. *Micromachines* **8**, 206 (2017).

33. G. Yamamoto, T. Hashida, Carbon nanotube reinforced alumina composite materials, in *Composites and Their Properties*, N. Hu, Ed. (IntechOpen, 2012).

34. M. Rungta, C. Zhang, W. J. Koros, L. Xu, Membrane-based ethylene/ethane separation: The upper bound and beyond. *AIChE J.* **59**, 3475–3489 (2013).

35. S. M. Lai, L. T. Y. Au, K. L. Yeung, Influence of the synthesis conditions and growth environment on MFI zeolite film orientation. *Microp. Mesop. Mater.* **54**, 63–77 (2002).

36. P. Cubillas, M. W. Anderson, M. P. Attfield, Crystal growth mechanisms and morphological control of the prototypical metal–organic framework MOF-5 revealed by atomic force microscopy. *Chem. A Eur. J.* **18**, 15406–15415 (2012).

37. P. Y. Moh, P. Cubillas, M. W. Anderson, M. P. Attfield, Revelation of the molecular assembly of the nanoporous metal organic framework ZIF-8. *J. Am. Chem. Soc.* **133**, 13304–13307 (2011).

38. Z. Zhou, D. Guo, D. B. Shinde, L. Cao, Z. Li, X. Li, D. Lu, Z. Lai, Precise sub-angstrom ion separation using conjugated microporous polymer membranes. *ACS Nano* **15**, 11970–11980 (2021).

39. J. P. Verduijn, A. J. Bons, M. H. Anthonis, L. H. Czarnetzki, *Int. Pat. Appl. PCT* WO 96/01683 (1996).

40. L. Diestel, X. L. Liu, Y. S. Li, W. S. Yang, J. Caro, Comparative permeation studies on three supported membranes: Pure ZIF-8, pure polymethylphenylsiloxane, and mixed matrix membranes. *Microp. Mesop. Mater.* **189**, 210–215 (2014).

41. M. Stroet, B. Caron, K. M. Visscher, D. P. Geerke, A. K. Malde, A. E. Mark, Automated topology builder version 3.0: Prediction of solvation free enthalpies in water and hexane. *J. Chem. Theory Comput.* **14**, 5834–5845 (2018).

42. A. K. Malde, L. Zuo, M. Breeze, M. Stroet, D. Poger, P. C. Nair, C. Oostenbrink, A. E. Mark, An Automated Force Field Topology Builder (ATB) and repository: Version 1.0. *J. Chem. Theory Comput.* **7**, 4026–4037 (2011).

43. B. Zheng, M. Sant, P. Demontis, G. B. Suffritti, Force field for molecular dynamics computations in flexible ZIF-8 framework. *J. Phys. Chem. C* **116**, 933–938 (2012).

44. W. F. van Gunsteren, S. R. Billeter, A. A. Eising, P. H. Hünenberger, P. Krüger, A. E. Mark, W. R. P. Scott, I. G. Tironi, *Biomolecular Simulation: The GROMOS96 Manual and User Guide* (Hochschulverlag AG an der ETH Zürich, Zürich, Switzerland, 1996).

45. B. Hess, C. Kutzner, D. van der Spoel, E. Lindahl, GROMACS 4: Algorithms for highly efficient, load-balanced, and scalable molecular simulation. *J. Chem. Theory Comput.* **4**, 435–447 (2008).

46. D. Van Der Spoel, E. Lindahl, B. Hess, G. Groenhof, A. E. Mark, H. J. C. Berendsen, GROMACS: Fast, flexible, and free. *J. Comput. Chem.* **26**, 1701–1718 (2005).

47. E. Lindahl, B. Hess, D. van der Spoel, GROMACS 3.0: A package for molecular simulation and trajectory analysis. *Mol. Mod. Annu.* **7**, 306–317 (2001).

48. C. Oostenbrink, A. Villa, A. E. Mark, W. F. Van Gunsteren, A biomolecular force field based on the free enthalpy of hydration and solvation: The GROMOS force-field parameter sets 53A5 and 53A6. *J. Comput. Chem.* **25**, 1656–1676 (2004).

49. H. J. C. Berendsen, J. P. M. Postma, W. F. Vangunsteren, A. Dinola, J. R. Haak, Molecular-dynamics with coupling to an external bath. *J. Chem. Phys.* **81**, 3684–3690 (1984).

50. G. Bussi, D. Donadio, M. Parrinello, Canonical sampling through velocity rescaling. *J. Chem. Phys.* **126**, 014101 (2007).

51. W. Humphrey, A. Dalke, K. Schulten, VMD: Visual molecular dynamics. *J. Mol. Graph.* **14**, 33–38 (1996).

52. X. Yang, Z. Wen, Z. Wu, X. Luo, Synthesis of ZnO/ZIF-8 hybrid photocatalysts derived from ZIF-8 with enhanced photocatalytic activity. *Inorg. Chem. Front.* **5**, 687–693 (2018).

53. M. S. Dresselhaus, A. Jorio, M. Hofmann, G. Dresselhaus, R. Saito, Perspectives on carbon nanotubes and graphene Raman spectroscopy. *Nano Lett.* **10**, 751–758 (2010).

54. A. Jorio, R. Saito, Raman spectroscopy for carbon nanotube applications. *J. Appl. Phys.* **129**, 021102 (2021).

55. G. Xue, Q. Dai, S. Jiang, Chemical reactions of imidazole with metallic silver studied by the use of SERS and XPS techniques. *J. Am. Chem. Soc.* **110**, 2393–2395 (1988).

56. T. I. T. Okpalugo, P. Papakonstantinou, H. Murphy, J. McLaughlin, N. M. D. Brown, High resolution XPS characterization of chemical functionalised MWCNTs and SWCNTs. *Carbon* **43**, 153–161 (2005).

57. A. Theodosiou, B. F. Spencer, J. Counsell, A. N. Jones, An XPS/UPS study of the surface/near-surface bonding in nuclear grade graphites: A comparison of monatomic and cluster depth-profiling techniques. *Appl. Surf. Sci.* **508**, 144764 (2020).

58. H. K. Jeong, E. Echeverria, P. Chakraborti, H. T. Le, P. A. Dowben, Electronic structure of cyclodextrin–carbon nanotube composite films. *RSC Adv.* **7**, 10968–10972 (2017).